Surface excitations relaxation in the Kondo insulator $Sm_{1-x}Gd_xB_6$

J. C. Souza,[1,2,*] M. König,[2] M. V. Ale Crivillero,[2] M. O. Malcolms,[1] R. R. Urbano,[1] Z. Fisk,[3] P. F. S. Rosa,[4]
P. G. Pagliuso,[1] S. Wirth,[2] and J. Sichelschmidt[2]
[1]*Instituto de Física "Gleb Wataghin", UNICAMP, 13083-859 Campinas, São Paulo, Brazil*
[2]*Max Planck Institute for Chemical Physics of Solids, D-01187 Dresden, Germany*
[3]*Department of Physics and Astronomy, University of California, Irvine, California 92697, USA*
[4]*Los Alamos National Laboratory, Los Alamos, New Mexico 87545, USA*

(Received 13 April 2021; revised 8 June 2021; accepted 9 June 2021; published 2 July 2021)

The interplay between nontrivial topological states of matter and strong electronic correlations is one of the most compelling open questions in condensed matter physics. Due to experimental challenges, there is an increasing desire to find more microscopic techniques to complement the results of more traditional experiments. In this work, we locally explore the Kondo insulator $Sm_{1-x}Gd_xB_6$ by means of electron spin resonance (ESR) of Gd^{3+} ions at low temperatures. Our analysis reveals that the Gd^{3+} ESR line shape shows an anomalous evolution as a function of temperature, wherein for highly dilute samples ($x \approx 0.0002$) the Gd^{3+} ESR line shape changes from a localized ESR local moment character to a diffusive-like character. Upon manipulating the sample surface with a focused ion beam we demonstrate, in combination with electrical resistivity measurements, that the localized character of the Gd^{3+} ESR line shape is recovered by increasing the penetration of the microwave in the sample. This provides compelling evidence for the contribution of surface or near-surface excitations to the relaxation mechanism in the Gd^{3+} spin dynamics. Our work brings new insights into the importance of nontrivial surface excitations in ESR, opening new routes to be explored both theoretically and experimentally.

DOI: 10.1103/PhysRevResearch.3.033016

I. INTRODUCTION

The concept of topology in condensed matter physics emerged from breakthroughs in the quantum Hall effect [1]; however, more recently such a concept was generalized to other states of matter, such as topological insulators [2], Dirac and Weyl semimetals [3–5], and other exotic phenomena [6,7]. The gapless spin-polarized surface states of topological insulators were the first of these new states of matter to be explored, both theoretically and experimentally [2]. One of the most pressing questions that remains open is the role of topological states of matter in systems where electronic correlations are important, which are known as strongly correlated systems [8–12].

The prototypical material to study this interplay is the Kondo insulator SmB_6 [9,13,14]. Although extensively studied over the last 40 years, the prediction of a topological insulating ground state in this compound brought back interest in this system [15–22]. With a simple cubic structure (space group $Pm\bar{3}m$), SmB_6 has all the properties required of a cubic topological Kondo insulator (TKI), such as the Γ_8 quartet crystal field ground state and an odd number of band inversion at the X point in the Brillouin zone [14,17,23]. The hybridization between the d conduction electrons and the Sm-4f electrons opens a gap at the Fermi energy, and the system becomes a good insulator at low temperatures [24,25]. In consequence, the bulk carriers contribute less to the transport upon lowering the temperature and a plateau is observed in resistivity at low temperatures, which is related to surface states dominating the conductivity [15,25–28]. An additional energy scale inside of the hybridization gap in scanning tunneling spectroscopy has been linked to these surface states [29–31].

Although the surface states are well established, there is still debate about their topological nature. Although recent quasiparticle interference and angle-resolved photoemission spectroscopic results demonstrated compelling evidence of nontrivial topology [14,18,20,21,31,32], other reports argued that a trivial surface state is at play [33,34]. Recent results showed that the Kondo insulating state was very sensitive to disorder [35–39], which indicated that the observed difference may be accounted for by subtleties in growth conditions [13,40–45]. Although natural impurities, such as Gd^{3+}, locally affect the hybridization gap, highly dilute concentrations do not globally affect the Kondo insulating phase [39,46]. In particular, $Sm_{1-x}Gd_xB_6$ samples with $x = 0.0002$ exhibit insulating behavior at low temperatures [47]. In this scenario, the use of a spectroscopic technique to complement the recent experimental results is highly desirable. Although electron spin resonance (ESR) is a bulk sensitive measurement, the microwave penetration into the sample can be affected by both surface and bulk conductivity. Furthermore, the resonance energy absorbed by the probe spin may ultimately relax

---

[*] jcsouza@ifi.unicamp.br

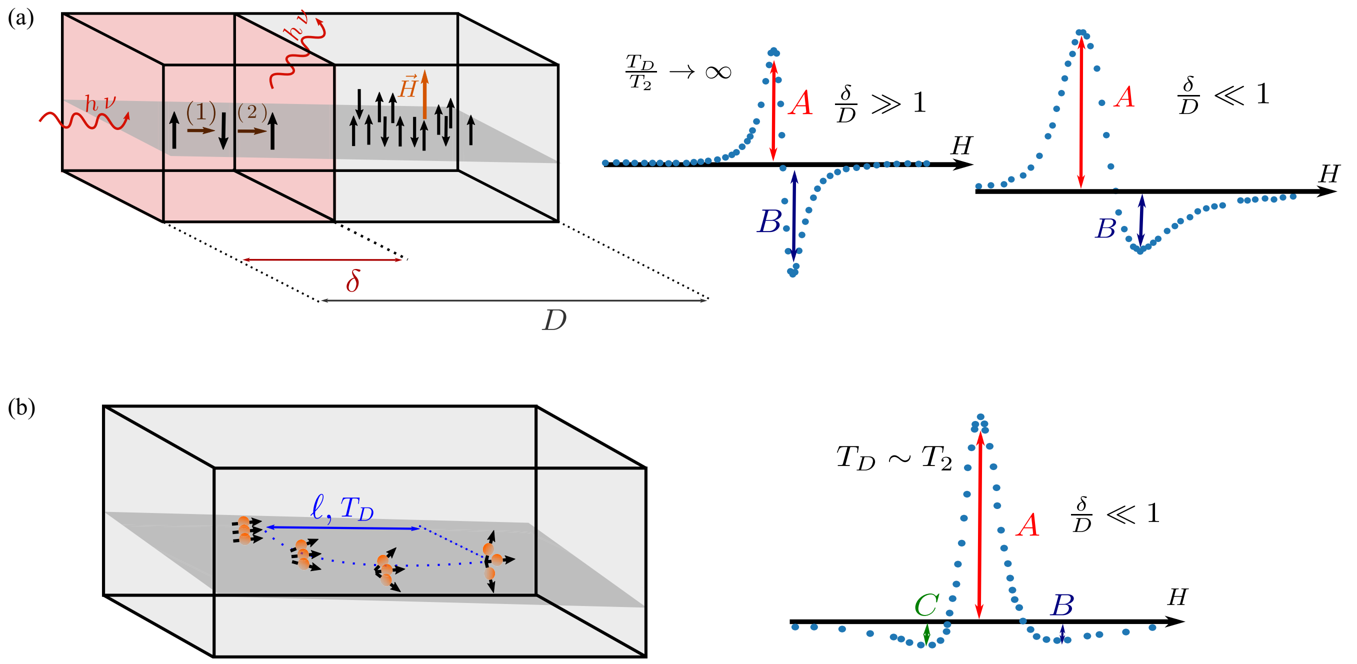

FIG. 1. (a) Pictorial representation of a local moment ESR of a $S = 1/2$ probe, where δ is the skin depth, D the thickness of the sample, T_D the diffusion time, and T_2 the spin-spin relaxation time. ↑ represents the $|\uparrow\rangle$ ground state and ↓ the $|\downarrow\rangle$ excited state. The orange vector **H** shows the externally applied magnetic field direction. $\delta/D \gg 1$ is an insulator (symmetric "local"line shape) and $\delta/D \ll 1$ is a metal-"local"line shape with "skin asymmetry."(b) Pictorial semiclassical representation of the interplay between the coherence loss of the spin system (T_2) and the diffusion of the spin system (T_D, which is connected with the mean free path ℓ) for a sample showing a CESR. The line shape represents the CESR case when $T_D \sim T_2$ (line shape with "diffusive asymmetry"). The dotted line in the left panel illustrates the spatial shift of the carrier. For simplicity we do not present the concomitant spin-lattice relaxation of the spin system. The ESR spectra in (a) and (b) are plotted as the power absorption derivative (dP/dH) as a function of the magnetic field H and were adapted from [51–53] for the insulator, metal, and conduction-electron cases, respectively.

through the surface to the thermal bath, which makes ESR also surface sensitive [48–50].

The relation between ESR properties and sample conductivity has been investigated for the case in which diffusion of spin excitations becomes relevant [54]. Dyson demonstrated early on [55] that the line shape can basically be influenced by two effects: the skin effect, through the ratio of the skin depth δ to the sample thickness D, and the diffusion of the resonating magnetic moments, through the ratio between diffusion time T_D and the spin-spin relaxation time T_2. On one hand, the former is a result of the interplay of the microwave field and the carriers, where shielding currents drive electromagnetic fields out of phase [51,54,56,57]. On the other hand, the latter is a measure of the coherence loss of the resonating spins [54,56,57].

The case for a local moment ESR is pictorially represented in Fig. 1(a) for a simple $S = 1/2$ system. An external magnetic field splits the degenerated spin state into a spin-up ground state $|\uparrow\rangle$ and a spin-down excited state $|\downarrow\rangle$. Microwave energy matching this energy splitting can be absorbed [process (1)] and emitted [process (2)]. A net absorption, and therefore an observable ESR signal, is possible when the spin system relaxes energy from $|\downarrow\rangle$ to the thermal bath. Here, two different and simultaneous relaxation mechanisms are involved: the already mentioned spin-spin relaxation and the spin-lattice relaxation, which is connected to the energy transfer through phonons to the thermal bath with a characteristic timescale T_1 [58–60].

The skin effect and the diffusion of spin excitations lead to distortions of the line shape, which can be measured by the amplitude ratio A/B as shown in Fig. 1—the ESR spectra were adapted from [51–53]. In the almost completely stationary regime of local moment ESR, i.e., $T_2 \ll T_D$, the symmetry of the line shape is only defined by the ratio $\lambda = \delta/D$ [48]. As shown in the center panel of Fig. 1(a) for insulators, where $\lambda \gg 1$, one obtains a symmetric Lorentzian line shape with $A/B = 1$. In metals, where $\lambda \ll 1$, the skin depth effect will be more relevant and a so-called Dysonian line shape occurs, which has a "skin asymmetry" and an upper limit $A/B \approx 2.7$ [48,54]. The differences between insulators and metals are further manifested in the relaxation of the system, which can be explored by measuring the saturation of the ESR intensity as a function of the microwave power, where insulators saturate at much lower microwave powers when compared with conductors [56].

Figure 1(b) depicts in a semiclassical way the case for a conduction-electron spin resonance (CESR), where T_D can be comparable in some cases to T_2. The interplay between the coherence loss and the diffusion of the spin system plays an important role on the ESR line shape. While the coherence loss, as governed by T_2, macroscopically results in the loss of the transverse magnetization, the diffusion, characterized by

T_D, is connected with the mean free path ℓ. A line shape with a "diffusive asymmetry" is obtained for $T_D \sim T_2$, resulting in $A/B \geqslant 2.7$ and an additional C valley in the shape, as defined in Fig. 1(b). If $T_D \sim T_2$, the spin probe has a significant probability of a considerable spatial shift before the coherence between the probe spins is lost. Therefore, there is a diffusion of the spin excitations within the layer induced by the skin effect, which results in a diffusive line shape, shown in the right panel of Fig. 1(b). The spin-lattice relaxation, which macroscopically results in the recovery of the longitudinal magnetization, is not represented in Fig. 1(b) for simplicity. In systems with a mean free path greater than the skin depth, i.e., $\ell/\delta \geqslant 1$ (anomalous skin effect), the ratio C/B can be larger than 1 [61].

Recently, highly unusual ESR line shapes were reported for the half-Heusler compounds YPtBi and YPdBi substituted with Nd^{3+} [49,62]. The Nd^{3+} ESR line shape showed a diffusive asymmetry although the Nd^{3+} spins are localized. This diffusive asymmetry was discussed to be an experimental signature of nontrivial topological states. It was related to a relaxation mechanism through Dirac excitations in or near the surface by virtue of a so-called phonon-bottleneck effect, which results in an enhanced spin-lattice relaxation time T_1 [58–60,63]. In this case, the absorbed energy would diffuse through the surface before relaxing to the thermal bath.

In this work, we report the observation of a diffusive asymmetry in the Gd^{3+} ESR line shape of highly dilute Gd^{3+}-substituted SmB_6. Combining microwave power-dependent ESR, focused ion beam (FIB) for cutting trenches on the sample surface, and complementary resistivity measurements, we provide evidence for surface excitations contributing to the ESR relaxation. The FIB treatment of the sample surface results in an increase of the skin depth, i.e., the microwave penetration and the recovery of a local ESR line shape [49]. Our temperature and FIB dependencies of the diffusive-like line shape and the Gd^{3+} ESR spin relaxation provides strong evidence that surface and near-surface excitations, in the presence of a phonon bottleneck regime, are crucial ingredients to obtain such an unusual effect in an ESR experiment. As this system has been claimed to have metallic surface states [14,18,21,31,32], these surface excitations are likely to be electronic.

II. METHODS

Single crystalline samples of $Sm_{1-x}Gd_xB_6$ ($x = 0.0004$ and 0.0002) were synthesized by the Al-flux growth technique with starting elements Sm:Gd:B:Al in the proportion of $(1-x)$:x:6:600 [13,44,64]. The samples ranged in size from ~0.7 to 1.4 mm width, 300- to 900-μm length and 120- to 500-μm thickness. Laue measurements confirmed the (001) planes of the largest facets. The x used in the text refers to the nominal Gd^{3+}-concentration value. The magnetic properties of $x = 0.0002$ samples were obtained using a vibrating sample magnetometer equipped with a superconducting quantum interference device (SQUID-VSM). Electrical resistivity was measured using a four-point technique with van der Pauw geometry.

The crystals were etched before the first ESR measurement in a dilute mixture of hydrochloric and nitric acids in a proportion of 3:1 to remove possible impurities on the surface of the crystals due to Al flux. We did not polish any of the crystals in this study. For $x = 0.0002$ we show the results of two different crystals (S1 and S2). The ESR measurements were performed on single crystals in an X-band ($\nu \cong 9.4$ GHz) spectrometer equipped with a goniometer and a He-flow cryostat in the temperature range of 2.6 K $\leqslant T \leqslant$ 40 K at powers of 0.2μW $\leqslant P \leqslant$ 10 mW. The ESR spectra were analyzed using the software SPEKTROLYST.

To investigate the dependence of the ESR line shape on the surface properties, we employed a focused ion beam (FIB) for surface treatment using a Xe ion beam with currents of 500 nA and acceleration voltage of 30 kV. It turned out that this technique can change the surface conductivity in a systematic way, in contrast to just using a hand-made surface scratch [47]. In each FIB treatment we cut linear trenches of about 7–10 μm depth into the sample surface, resulting in a grid of such trenches with ever-increasing density. In the first two treatments we divided the sample in four equal parts (F1 and F2). In subsequent runs we approximately doubled the number of lines in each direction [47]. We investigated the ESR after each new FIB cut. We also performed energy dispersive x-ray spectroscopy in regions which were milled a few μm into the bulk. It was possible to only detect the signals of Sm, B, and O, with Gd being below the detection limit (usually ~1%) [47]. Interestingly, after milling no Al signal could be detected, indicating that the Al content in the bulk, if any, is below the detection limit, which differs from, e.g., UBe_{13} [65].

III. RESULTS

Figure 2(a) shows a fine-structure split Gd^{3+} ESR spectrum at $T = 4$ K for $Sm_{1-x}Gd_xB_6$ ($x = 0.0004$) with applied magnetic field H parallel to the [100] direction. The well-resolved fine-structure is characteristic of spin probes immersed in the insulating sample bulk allowing the weak crystalline electric field (CEF) of the Gd^{3+} ions to split the line [54,57]. Gd^{3+} substitute Sm ions, which have a cubic local symmetry. As such, a cubic CEF effect is expected for Gd^{3+} ions. In fact, the red solid line is a simulation with seven resonances considering a cubic CEF spin Hamiltonian with a Gd^{3+} crystal field parameter $b_4 = -9.5(3)$ Oe [39]. Two pairs of fine-structure transitions are close in energy, which results in weak shoulders. To analyze our ESR line without the fine-structure influence, we turned the sample by 30 degrees away from the [001] towards the [110] direction until the Gd^{3+} ESR spectrum is collapsed into one Gd^{3+} resonance line [54,57] as shown in Fig. 2(b). The red solid line is the best fit with a Lorentzian line shape, which is expected for an insulator.

Figure 2(c) shows the Gd^{3+} ESR spectrum for $x = 0.0002$ at $T = 3.6$ K for H parallel to the [100] direction (sample S1). Again we observe seven resonances, which reinforces the notion that we are probing the bulk of SmB_6. However, we cannot reproduce our spectrum by using a local-type line shape with skin asymmetry ("Dysonian")—see the magenta solid line. The difficulties in adjusting the data with a fine-split Dysonian line shape becomes even clearer when we collapse the spectrum into one line, as shown by the magenta solid line

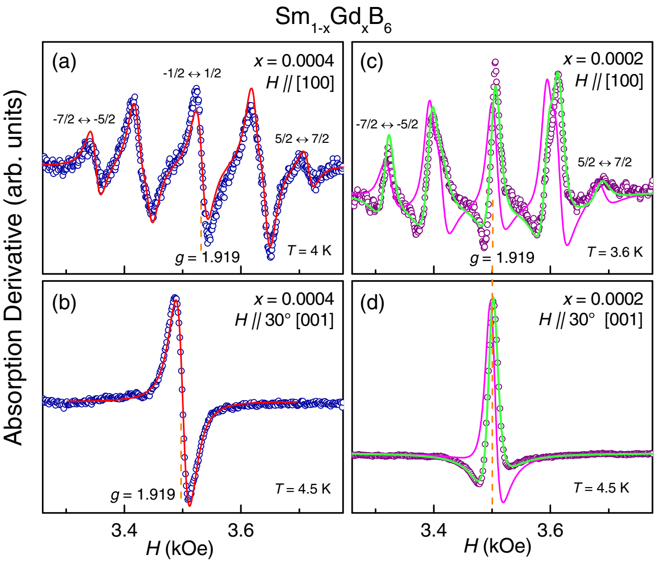

FIG. 2. Gd^{3+} ESR spectrum for H applied parallel to the [100] direction and the Gd^{3+} collapsed spectrum for (a), (b) $x = 0.0004$ and (c), (d) $x = 0.0002$ in $Sm_{1-x}Gd_xB_6$. The red, magenta and green solid lines are explained in the text. Two pairs of transitions ($\pm5/2 \rightarrow \pm3/2$ and $\pm3/2 \rightarrow \pm\ 1/2$) in (a) and (c) are close in energy, which results in a weak shoulder in the left and right middle lines. The orange dashed lines show the g-value = 1.919, which is characteristic of Gd^{3+} ions highly diluted inside a SmB_6 matrix [39]. Gd^{3+} ESR spectra for $x = 0.0004$ have been adapted from [39].

in Fig. 2(d). However, as demonstrated by the green lines, a diffusive asymmetry in the line shape (C-valley > 0) of the Gd^{3+} ESR describes the spectra very well. This is highly unusual for a Gd^{3+} spin probe that is expected to be localized in SmB_6.

To quantify the development of this diffusive asymmetry, we propose an analogy to a model of a CESR in the presence of an anomalous skin effect [61]. In this model, the ESR spectrum, which is expressed by the power absorption derivative (dP/dH) as a function of H, can be described as

$$\frac{dP}{dH} \propto [1 - (X/R)^2]\frac{d}{dx}\left(\frac{1}{1+x^2}\right) + (2X/R)\frac{d}{dx}\left(\frac{x}{1+x^2}\right), \tag{1}$$

where $x = 2(H - H_r)/\Delta H$, with H_r as the resonance field and ΔH as the line width [48]. The X/R parameter in this CESR model is directly connected with the surface impedance, where R is the surface resistance and X the surface reactance [61,66]. For $X/R = 0$ we have a symmetric Lorentzian line shape ($A/B = 1$), whereas $X/R = \sqrt{2} - 1$ corresponds to a Dysonian line shape ($A/B \approx 2.7$). Finally, $X/R\ \geqslant 1$ occurs when the anomalous skin effects play a role ($C/B\ \geqslant 1$) [61].

The green solid line in Fig. 2(c) is a simulation assuming the same parameters for the g-values and b_4 from the red solid line in Fig. 2(a) and using $X/R = 1.6$. For the Gd^{3+} collapsed spectrum, shown in Fig. 2(d), we exclude the influence of the crystal field, therefore we can fit our data using Eq. (1). Again we maintained the same g-value and ΔH of the red solid line and obtained a $X/R\ \approx 1.3$. The simulation and the fit reproduce nicely the unusual spectra shape, which in case of a CESR would indicate that spin diffusion is relevant in the relaxation process. However, we recall that in $Sm_{1-x}Gd_xB_6$ ESR does not probe conduction electrons and, therefore, X/R here is just a mathematical parameter. It is important to note that in Fig. 2(c) a significant diffusive asymmetry is present in each of the fine-split Gd^{3+} lines, confirming again their origin from Gd^{3+} ions in the bulk of SmB_6.

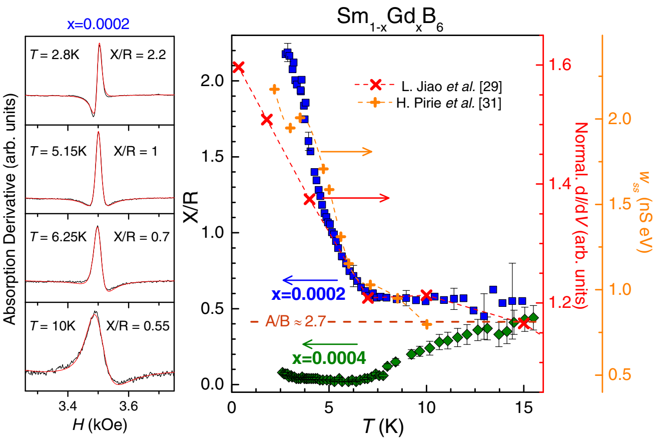

FIG. 3. Temperature dependence of Gd^{3+} ESR spectra and line shape parameter X/R in $Sm_{1-x}Gd_xB_6$. All the Gd^{3+} ESR spectra were taken with a microwave power smaller than the saturation of the system. Left panel: ESR spectra (black lines) for $x = 0.0002$ at various temperatures and spectra fits (red lines) by Eq. (1) with X/R parameters as indicated. Right panel: Temperature dependence of X/R for $x = 0.0002$ and $x = 0.0004$. A localized character of the line shape occurs below the brown dashed line which indicates a line shape asymmetry of $A/B \approx 2.7$. The red (orange) symbols show the $V_b = -6.5$ meV (-5 meV) scanning tunneling spectroscopy peak intensity obtained in a nonreconstructed (reconstructed) B- (Sm-) terminated surface for SmB_6 reported previously [29] ([31]). The orange and red dashed lines are just guides to the eyes.

One possible explanation for the diffusive asymmetry could rely on an electrodynamics effect leading to an unconventional mixing of absorption and dispersion parts of the Lorentzian line shape in Eq. (1). Such an explanation could be based on highly conductive surfaces on top of an insulating bulk causing a large phase shift in the microwave response, making the dispersion to dominate. However, such an interpretation, which is not consistent with Dyson's theory [48,55], has not been observed experimentally and is not supported by at least two other previous experimental observations. The first, and most important, is the coexistence of localized and diffusive ESR line shapes in half-Heusler systems [49,62,67]. Another important example is the local-moment ESR spectra in superconductors, which have highly conducting surfaces and do not show a diffusive-like character [68–72]. Instead, as expected from Dyson's theory, the maximum A/B ratio is $\approx$2.7 [48,54,55]. Both examples support the notion that in $Sm_{1-x}Gd_xB_6$ the strong and peculiar asymmetry of the Gd^{3+} line shape does not arise from an electrodynamics effect of the inhomogeneous conductivity cross section of the sample.

The right panel of Fig. 3 shows the temperature evolution of the collapsed Gd^{3+} ESR spectra diffusive parameter X/R for $Sm_{1-x}Gd_xB_6$ with $x = 0.0002$ (sample S1) and

$x = 0.0004$. A similar evolution has been found for each line of the fine-split spectra at $H \| [100]$ (Appendix D). At temperatures exceeding $T \approx 12$ K, where the transport is dominated by carriers in the bulk of the sample [24,29,39], both samples show $X/R \sim 0.5$, which indicates a localized-like behavior of the Gd^{3+} ESR spectra, i.e., a line shape with a skin asymmetry, $A/B \approx 2.7$. For $x = 0.0004$, the expected development towards a symmetric Lorentzian line shape ($X/R \sim 0$) is observed at low temperatures, which is typical due to the insulating nature of the bulk. For $x = 0.0002$, at these temperatures, we should expect for X/R a similar value, or at most $X/R \sim 0.5$ if the sample size is larger compared to the skin depth. However, for $x = 0.0002$ the X/R parameter strongly increases below $T \approx 6$ K. This evolution is also clearly visible in the spectra as shown in the left panel of Fig. 3. The decrease of the growing rate of the X/R parameter towards the lowest temperatures should be taken with care due to the increase of error bars for higher X/R values.

The X/R temperature evolution is reminiscent of a signature peak in scanning tunneling spectroscopy studies. For comparison, the temperature dependencies of the intensity of the $V_b = -6.5$ meV and -5 meV peaks are also included in the right panel of Fig. 3 (red and orange data points) [29,31]. The peaks, measured in a nonreconstructed B-terminated (-6.5 meV) and in a reconstructed Sm-terminated SmB_6 surfaces (-5 meV), were correlated to the surface states in pristine Al-flux grown samples [29,31]. As argued by Jiao *et al.*, the clear change of the T-dependence of the intensity of the -6.5-meV peak relies on the formation of the metallic surface states [29].

The correlation between the evolution of both peaks, from differently terminated surfaces, and the evolution of a diffusive asymmetry of the line shape hints to the relevance of the surface states of SmB_6 in the Gd^{3+} ESR line shape. In this respect, we should expect a relaxation mechanism including a coupling between the bulk Gd^{3+} impurities and the surface states. Such a coupling should be mediated by a relaxation through the phonons, which causes an enhancement of the spin-lattice relaxation time T_1 [49]. Therefore, it would be helpful to tune the diffusive asymmetry of the Gd^{3+} ESR line shape to construct an appropriate relaxation scenario. To this end, we changed the surface properties using a focused ion beam. A detailed resistivity study of the FIB effects can be found in [47]. Another important tuning parameter is the Gd^{3+} concentration, which can be a source to understand the role of disorder in the diffusive asymmetry of the line shape [39].

Figure 4(a) exemplifies one of the stages of the FIB cuts in sample S2. As shown in Fig. 4(b), at $T = 3.8$ K, there is a systematic change of the Gd^{3+} diffusive-like line shape as a function of the FIB grid, which finally results in a Gd^{3+} localized-like (skin asymmetric) line shape after the final removal (F11), in which no distinct trenches were cut but rather an approximate 5-μm thick layer was FIB-sputtered from the complete surface. We must notice that, as shown in Table I in Appendix B, the g-value and the Gd^{3+} linewidth remain unchanged within our experimental uncertainty as a function of the FIB grid.

Figure 4(c) presents the temperature evolution of the X/R parameter for $T \leqslant 6.5$ K and for selected FIB grids for $\mathrm{Sm}_{1-x}\mathrm{Gd}_x\mathrm{B}_6$ ($x = 0.0002$). At $T \geqslant 5$ K for the first few FIB grids it was possible to observe $X/R > 0.5$, i.e., a diffusive asymmetry of the line shape. With increasing FIB grid, X/R is systematically reduced. As shown in Fig. 3, the scanning tunneling peaks associated with the surface states are still present at these temperatures [29,31]. As such, we can expect that surface states may still play a role at these temperatures. For $T \leqslant 5$ K we can see a systematic drop of the X/R parameter as a function of the FIB cutting. The evolution of the Gd^{3+} diffusive asymmetry is heavily suppressed as a function of the FIB-cutting grid.

Figure 4(d) shows the Gd^{3+} ESR intensity as a function of the FIB grid. This intensity is not only proportional to the Gd^{3+} concentration but also to the interactive volume V^{int} which, in a first approximation, is given by $V^{\mathrm{int}} = \sigma\delta$, with σ being the surface area of the crystal. We further assume that the FIB cutting has a small effect on the total volume of the sample, which can be included in the error bar. As shown in Fig. 4(d), there is a systematic increase of the Gd^{3+} ESR intensity and, hence, the interactive volume as a function of the FIB grid. In other words, the skin depth gets larger as a function of increasing number of FIB-cut lines. At the same time, the X/R development indicates an evolution from a diffusive to a skin asymmetry of the line shape. This is an important hint that surface effects should be considered as an essential ingredient to the unusual diffusive asymmetry of the line shape. The increase of the skin depth suggests a FIB-induced depletion of the surface states, which effectively increases the surface resistivity [47]. Such an increase may be related to confinement of surface states or even disorder [37,38,73]. Disorder may also affect, for example, the Sm valence near the surface [74,75].

The presence of conducting surface states has been demonstrated to be the origin of the resistivity plateau in SmB_6 [16,22,26]. Therefore, as a matter of comparison, we also measure the dc resistivity ρ of the same ESR-investigated samples as a function of temperature for different FIB cutting-grids as shown in Fig. 4(e) [47]. The value of the low-temperature resistivity plateau continuously increases with the grid of the FIB cuttings. Hence, in the low-temperature regime, for a FIB-treated sample surface, the contribution of the surface states to the overall conduction appears to be suppressed. Accordingly, the skin depth as determined from the resistivity should be affected as well. Using a two-layered model, where we consider that the conducting carriers at the surface are the main contributors to the resistivity at low temperatures (more details in Appendix B) [26,27], we show that there is a systematic increase of the skin depth and a decrease of the mean free path ℓ as a function of the density of FIB-cut trenches (Table I in Appendix B). Therefore, the increase of the skin depth estimated by dc resistivity and Gd^{3+} ESR intensity [Fig. 4(d)] are consistent. However, when comparing skin depth results from both methods one must bear in mind that for ESR the local resistivity is the only relevant factor, while a nonlocal (global) character prevails in resistivity. It is therefore more sensitive to extrinsic effects, such as subsurface cracks, dislocations, and any residual flux [24,25,47,76,77] while local ESR measurements are not strongly influenced by these extrinsic effects.

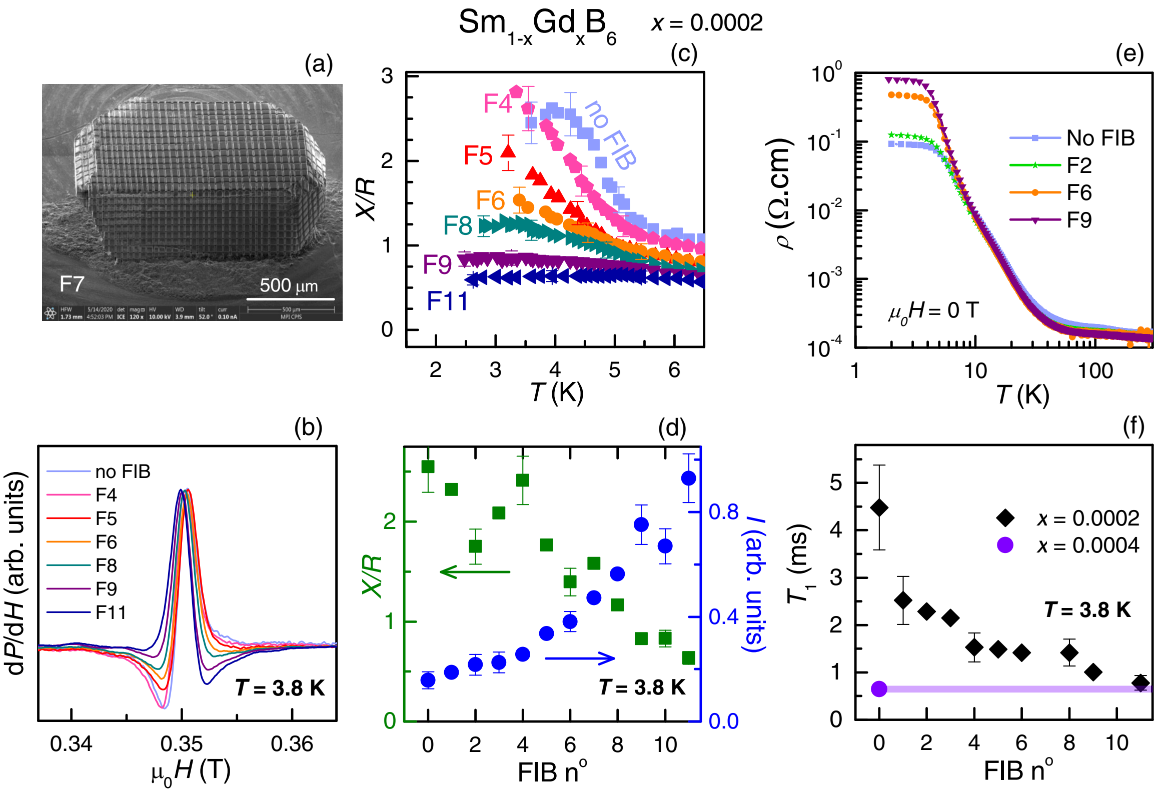

FIG. 4. (a) Scanning electron microscopy image of the $Sm_{0.9998}Gd_{0.0002}B_6$ sample S2 with intentional cuts made using a FIB. (b) Gd^{3+} ESR spectra at $T \approx 3.8$ K as a function of the FIB grid. The spectra were normalized to make the ESR line shapes comparable. (c) X/R line shape parameter as a function of temperature for different FIB cutting grids. (d) FIB cutting-grid dependence of X/R parameter and Gd^{3+} ESR intensity at $T = 3.8$ K. (e) Resistivity of sample S2 as a function of FIB cutting grid. Figure adapted from [47]. (f) Spin-lattice relaxation time T_1 as a function of FIB cutting for $x = 0.0002$ and 0.0004.

IV. DISCUSSION

So far our results have shown a compelling relation between the conducting sample surface, as clearly indicated by the low-T resistivity and changes of the skin depth, and the highly unusual Gd^{3+} ESR line shape in $Sm_{1-x}Gd_xB_6$. In analogy to the case of CESR, the Gd^{3+} line shape could be described by a parameter X/R defining a diffusive asymmetry. However, the spin probes themselves are not diffusing but their spin excitations do. To understand in more detail such a relaxation mechanism, we should look into the relevance of the surface effects in the spin-lattice relaxation T_1.

In metals, the relaxation of the spin probe is reflected in the linewidth, which is proportional to $1/T_2$ [54]. However, here we have a low-T bulk insulator and therefore, any evolution of the relaxation of the system should not necessarily be reflected in T_2, but in the spin-lattice relaxation T_1. As such, from the saturation behavior of the ESR intensity I as a function of the microwave power we can indirectly estimate T_1 (for more details see [56] and Appendix C). Figure 4(f) displays T_1 as a function of the FIB grid. As a matter of comparison, an estimated T_1 for $Sm_{1-x}Gd_xB_6$ with $x = 0.0004$, for which the line shape shows no diffusive asymmetry, is also presented.

The latter comparison reveals a distinct Gd-concentration dependence of T_1. The minute substitution of Sm by Gd results in a local modification of the Kondo lattice of SmB_6 and, hence, in a local reduction of the hybridization gap [39,78]. This additional disorder gives rise to an extra relaxation channel and reduces T_1 in an effectively similar way as in the opening of a bottleneck process [54]. With T_1 being too small due to extra relaxation channels, the line shape is of a localized type.

Looking now in Fig. 4(f) for $x = 0.0002$ at the FIB effects on T_1 and comparing them with the intensity (reflecting the skin depth) shown in Fig. 4(d), we can see that the increase of the skin depth is related to a decrease of the effective T_1. This finding may have two possible origins. The first one is that the cuts at the surface introduce incoherent (disorder) scattering, which diminishes the spin-lattice relaxation time at the surface.

The other one is related with the importance of relaxations due to the surface as such. Surface relaxations are important whenever there exist strong spin-dependent forces, i.e., spin polarization, during a collision of the spin excitation with the surface [48]. Dyson treated this modification briefly and showed that in the case of thin films or small particles, one expects a much more marked effect than in bulk materials [55]. In other words, the increase of the microwave penetration and the decrease of the mean free path ℓ, both FIB-induced effects, make the surface relaxation less relevant, which would result in a strongly reduced diffusive asymmetry of the line shape.

The analogies between the ESR line shape characters of conduction electrons and Gd^{3+} in SmB_6 are sensible and, hence, constitute a valuable basis for constructing our

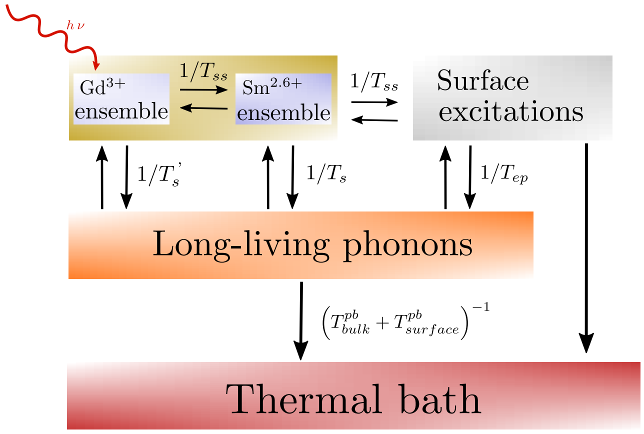

FIG. 5. Schematic representation of the proposed relaxation mechanism. $1/T_{\mathrm{ss}}$ represents a spin-spin relaxation rate, $1/T_s$ the spin-phonons relaxation, $1/T_{\mathrm{ep}}$ the relaxation through an electron-phonon coupling at the surface, and $T^{\mathrm{pb}}_{\mathrm{bulk}}$ the time scale of the phonons decoherence from the bulk and $T^{\mathrm{pb}}_{\mathrm{surface}}$ the timescale of the surface phonons decoherence.

relaxation mechanism which results in the Gd^{3+} diffusive-like line shape. To this end, it is instructive to first recall how a phonon bottleneck process could be responsible for the coupling between local moments and the surface excitations [49,63]. In a phonon bottleneck process, the phonons emitted by a direct process will be reabsorbed by the magnetic ions in the lattice [63]. This is a long-memory effect, meaning that it will result in an effective increase of the spin-lattice relaxation time T_1. This increase of T_1 can be interpreted as an increase of the phonon momentum coherence, which we will call long-living phonons [59,60]. In fact, such a spin-phonon process has already been demonstrated experimentally [79]. In this sense, the increase of the phonon coherence could enhance the probability of an energy transfer to surface excitations prior the relaxation to the thermal bath.

Figure 5 illustrates the various intermediate processes we propose for the total spin-lattice relaxation $1/T_1$. In this scenario we also take into account the relaxation through the surface. The Gd^{3+} relaxation to the phonons is realized through its crystal field [59,60], which is represented by the rate $1/T_s'$, where T_s' is the relaxation time from the spin probe to the phonons. Because Gd^{3+} has zero orbital momentum ($L = 0$), such coupling will not be so relevant. Now, we posit that the only reason that it is possible to see the diffusive asymmetry lineshape in Gd^{3+}-substituted SmB_6 is due to the Gd^{3+}–$Sm^{2.6+}$ coupling which was discussed in [39]. Because of their large concentration and $L \neq 0$, Sm ions have a much more efficient coupling, $1/T_s \gg 1/T_s'$, with long-living phonons. Such coupling between a concentrated Sm matrix with the phonons results in a phonon-bottleneck process and, concomitantly, an enhancement of T_1.

Whenever the transferred energy, through the phonons and even $Sm^{2.6+}$ ions, reaches the surface there is an impedance in the thermal exchange with the thermal bath, which is denoted by $(T^{\mathrm{pb}}_{\mathrm{bulk}} + T^{\mathrm{pb}}_{\mathrm{surface}})^{-1}$, where *pb* denotes phonon bottleneck. Due to this impedance it is possible to obtain a coupling of the surface phonons, or even the surface Sm ions, to the surface excitations, which effectively results in a diffusion of the magnetization while the system relaxes to the thermal bath.

One key question is related to the nature of the surface excitations. Indeed, one may argue that they not necessarily need to have a topological, or even an electronic nature. Clearly, without a proper model, which is beyond the scope of this work, we cannot rule out this scenario, but it seems unlikely. There are few points in favor of electronic excitations being the crucial ingredient, probably with a topological character. First our results show a compelling correlation between electrical conductance attributed to surface states and the evolution of the Gd^{3+} ESR line shape. One should also mention the T dependence for $T \leqslant 4$ K of the X/R parameter, especially for the sample without FIB-cut trenches, denoted as “no FIB” in Fig. 4(c). It shows, around $T \approx 4$ K, a reduction of the increase of the X/R parameter, which even appears to saturate. This happens right at the temperature where the surface states start to dominate the resistivity measurements. A similar situation is observed for sample S1, as shown in Fig. 3, where at low T there is a slight change in the increase of X/R. Although the analysis of X/R for $T \leqslant 4K$ should be taken with caution without a proper model, this is another hint of the connection between surface states and the Gd^{3+} ESR line shape.

The second point in favor of nontrivial electronic excitations is the comparison of Nd^{3+}-substituted YPdBi and YPtBi [49,62]. They show clearly different robustness of the diffusive line shape against external parameters (such as grain size and Nd^{3+} concentration). With both having a similar skin depth, and similarly enhanced T_1’s, in principle, a similar robustness of the diffusive asymmetry of the line shape should be expected for the two systems if phonons or electronic trivial excitations were responsible for the diffusive asymmetry; however this is not observed experimentally [49,62].

At this point it is worth returning to the tuning parameters and understand their role in light of our proposed relaxation mechanism scenario. Regarding the skin depth change, the decrease of the mean free path may diminish the spin-lattice relaxation time at the surface, which is denoted by $T^{\mathrm{pb}}_{\mathrm{surface}}$. The reduction of the surface relaxation time diminishes the probability of energy transfer to surface excitations. In other words, the role of the surface excitations to the relaxation of the system is suppressed as a function of the FIB cutting grids. Such suppression results in a decrease of the diffusive asymmetry, which is reflected in the X/R parameter, eventually leading to a Gd^{3+} localized-like line shape.

Another explored parameter is the Gd^{3+} concentration. Samples with $x = 0.0004$ of Gd^{3+} show a plateau in resistivity at low T [39], however, we speculate that in $x = 0.0004$ the number of Gd^{3+} ions is too high for a relaxation through the surface excitations. Moreover, one should not forget disorder effects. The additional disorder due to the increase of the Gd^{3+} concentration may suppress the spin-lattice relaxation, even at the surface, due to the creation of additional relaxation channels, which introduces incoherent scattering. This is nicely confirmed by the small T_1 for $x = 0.0004$ when compared with $x = 0.0002$ results. In fact, the FIB results, specifically those for small numbers of FIB-cut trenches, show that a tiny amount of disorder already creates effects in the line shape.

Finally, our work suggests that the highly diluted exchange ($x = 0.0002$) of $\mathrm{Sm}^{2.6+}$ ions by Gd^{3+} ions does not affect the local topology around the substituted sites. This is consistent with recent claims that a probe inside of a topological nontrivial matrix could not alter the topological nature of the system [80]. Our results demonstrate the influence of surface excitations in the relaxation of our ESR probe, which leads to an unusual diffusion asymmetry of the ESR line shape. Furthermore, they provide first hints that the unusual ESR line shape is likely related to the topological nature of the system.

V. CONCLUSION

In summary, we performed electron spin resonance and complementary resistivity measurements in the Kondo insulator $\mathrm{Sm}_{1-x}\mathrm{Gd}_x\mathrm{B}_6$ with $x = 0.0002$ and 0.0004. The Gd^{3+} ESR spectrum at $T = 4$ K for $x = 0.0002$ shows a diffusive-like character, which correlates with the temperature evolution of surface states in SmB_6. Using a focused ion beam we systematically altered the sample surface and showed the evolution of the Gd^{3+} ESR line shape from a diffusive-like to a localized-like character. Our analysis of the spin-lattice relaxation time T_1 reveals that the surface impedance opens the possibility of a diffusive asymmetry through nontrivial surface excitations. Further experiments in other systems and a theoretical description would be valuable to gain more insight to how electron spin resonance can be a smoking gun in the study of topological phases of matter.

ACKNOWLEDGMENTS

We thank Dieter Ehlers (University of Augsburg) for implementing fit functions in his SPEKTROLYST software package. This work was supported by FAPESP (SP-Brazil) Grants No. 2020/12283-0, No. 2018/11364-7, and No. 2017/10581-1; National Council of Scientific and Technological Development, CNPq Grants No. 309483/2018-2, No. 141026/2017-0, No. 442230/2014-1, and No. 304649/2013-9; CAPES Finance Code 001; and FINEP-Brazil and Brazilian Ministry of Science, Technology and Innovation. Z.F. acknowledges the funding from NSF-1708199. Work at Los Alamos National Laboratory (LANL) was performed under the auspices of the U.S. Department of Energy, Office of Basic Energy Sciences, Division of Materials Science and Engineering.

APPENDIX A: MAGNETIZATION MEASUREMENTS

Figure 6 represents the magnetic susceptibility as a function of temperature and the magnetization as a function of the applied magnetic field for $\mathrm{Sm}_{1-x}\mathrm{Gd}_x\mathrm{B}_6$ ($x = 0.0002$). The results for $x = 0.0004$ are reported elsewhere [39]. Assuming the Kondo single impurity model explored in [46], we estimated x to be ≈ 0.0002. This is in agreement with the rough comparison of the ESR intensity I for $x = 0.0002$ and 0.0004.

APPENDIX B: SKIN DEPTH AND MEAN FREE PATH

To understand the effects of the FIB-cut trenches, we examined the mean free path ℓ and the skin depth δ within a two-layered model [27,28]. The effective mean free path ℓ of carriers is given by

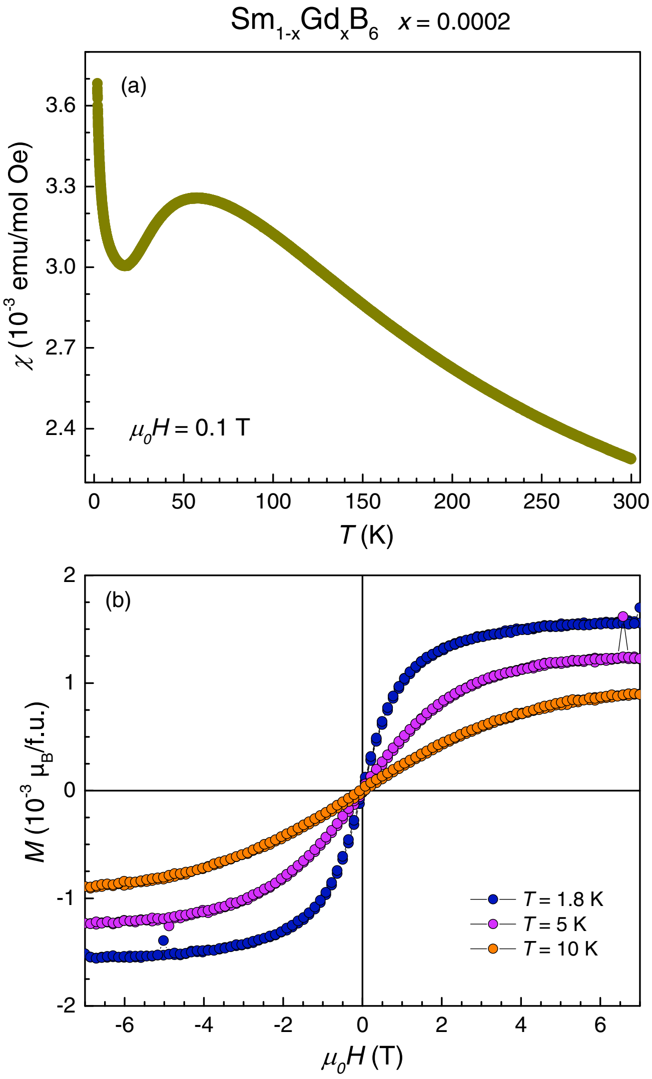

FIG. 6. (a) Magnetic susceptibility as a function of temperature and (b) magnetization as a function of the applied field for $\mathrm{Sm}_{1-x}\mathrm{Gd}_x\mathrm{B}_6$ ($x = 0.0002$).

$$\ell = \frac{m_e^* v_F}{ne^2\rho}, \tag{B1}$$

where m_e^* is the effective mass, v_F the Fermi velocity, n the carrier density, and ρ the resistivity of the sample. In light of the widespread values for n, m_e^*, and v_F for SmB_6 [25,31,32,41,42,44] absolute numbers should be taken with extreme care. However, in a first approximation, the trend of ℓ should be reliable because we should not have a relevant change in the carrier concentration as a function of the FIB-cut trenches.

Recent Corbino measurements demonstrated that the bulk resistivity of SmB_6 shows an insulating behavior at low temperatures [24]. Therefore, it is expected for the low-T regime that the conducting carriers are mostly in the surface layer [24,27]. With this assumption we use the carrier density of a two-dimensional layer $n_{2\mathrm{D}} \approx 2\times10^{14}$ cm^{-2} [25,27].

TABLE I. Experimental parameters extracted from resistivity and ESR measurements for sample S2. $\Delta y = (y - y^{F0})/y^{F0}$, where y can be ℓ, δ^{ρ_s}, or I, denotes the change of the respective parameter upon increasing the density of the FIB-cut trenches. $F0$ denotes the sample without FIB-cut trenches. We calculated δ^{ESR} assuming a 150-μm microwave penetration for F11. ΔH is the Gd^{3+} ESR linewidth and the g-value is extracted from the Gd^{3+} resonance field.

	ρ_{3D}^{2K} Ω cm	ρ_s $\mu\Omega$ cm	ℓ μm	$\Delta\ell$	δ^{ρ_s} μm	$\Delta\delta^{\rho_s}$	I arb. units	ΔI	δ^{ESR} μm	ΔH Oe	g-value
F0	0.092	2.67	3.8		0.85		39(8)		~ 25	16.5(9)	1.918(2)
F2	0.12	3.48	3.1	−0.21	0.97	0.14	47(8)	~ 0.2	~ 30	15.9(9)	1.919(2)
F6	0.47	13.6	0.78	−0.80	1.91	1.25	95(9)	~ 1.4	~ 60	16.8(9)	1.917(2)
F9	0.81	23.7	0.46	−0.88	2.53	1.98	190(20)	~ 3.8	~ 120	16.5(9)	1.918(2)
F11							230(20)	~ 4.9	150*	17.7(9)	1.918(2)

Further, on the basis of [25,31,32], we used $m_e^* \approx 410\ m_e$ and $v_F \approx 2.4\times10^3$ m/s.

Assuming that the conducting channel at the surface will be the most relevant at low T, the surface resistivity ρ_s is given by

$$\rho_s = \frac{2t_s}{G_{\mathrm{bulk}}} = \frac{2t_s\rho_{3\mathrm{D}}^{2\mathrm{K}}}{t}, \tag{B2}$$

where t_s is the surface states thickness, t the crystal thickness, G_{bulk} the bulk conductance and $\rho_{3\mathrm{D}}^{2\mathrm{K}}$ the resistivity value taken at $T = 2$ K. We used $t_s = 6$ nm [27] and $t = 410$ μm. Converting n_{2D} ($n = n_{2D}/t_s$) and using Eq. (B2) in Eq. (B1) we can estimate ℓ.

All the values are reported in Table I. There is a clear tendency of a reduction in ℓ as a function of the number of FIB-cut trenches due to the surface resistivity increase as a function of the increase of FIB cuts. As a matter of comparison, since the reported v_F values are quite widespread, we also used $v_F = 1.6\times10^5$ m/s [28] for an electron mass close to 1 m_e. In that case, we would obtain $\ell = 618$, 490, 125, and 73 nm for the pristine sample (F0), and for the FIB grades F2, F6, and F9, respectively. Although the absolute values are different, the tendency of the suppression of ℓ is the same.

Regarding the skin depth δ, the two-layered model is still relevant. To understand the effects of this highly conducting surface layer on the microwave penetration, we estimate the skin depth $\delta^{\rho_s} = \sqrt{\rho/\pi f \mu}$ within the surface layer. The results are reported in Table I.

Clearly, in these calculations, δ^{ρ_s} exceeds t_s by two orders of magnitude or more. Hence, despite the high conductivity, the incident microwave will have just a small attenuation due to the small t_s. As a consequence, our ESR spectra originate from the bulk, which is in accordance with the cubic fine-split Gd^{3+} ESR spectrum shown in Fig. 3. In this layered model, we are assuming, beyond the highly conducting surface, a higher bulk resistivity, which has an exponential behavior as a function of T for SmB$_6$ [24]. As such, the effective skin depth should be larger than this estimation, where we only took into account the surface layer. This is in agreement with a previous result which claims that the skin depth may be larger than the sample size for $x = 0.0004$ [39].

We can also estimate the relative skin depth increase from our ESR measurements upon progressing FIB cutting. As mentioned in the main text, as a first approximation, the ESR intensity I is directly proportional to the skin depth δ^{ESR}. Assuming $\delta^{\mathrm{ESR}} \sim 150$ μm for the last FIB grade F11, which is in accordance with previous estimations [39], we can estimate δ^{ESR} as a function of the numbers of the FIB-cut trenches. All values are reported in Table I.

At this point, it is highly interesting to compare trends of both δ^{ρ_s} and δ^{ESR} skin depth estimations—again we should emphasize that absolute numbers should be taken with extreme care. The qualitative agreement between the tendencies of both skin depths is clear. We see a quantitative agreement in the increase of the microwave penetration between F0 (which is the sample without FIB-cut trenches) and F2 and F6, however, there is a difference of a factor of 2 for F9.

This discrepancy may be related to the attenuation of the microwave being almost negligible at higher FIB grades. However, one should be aware of the following FIB effects which are not captured by our approach. The FIB cutting will result in surface damage extending several tens of nanometers into the crystal, thus, for example, inducing defects that may serve as dopants [47,81]. For a lower density of FIB-cut trenches, this effect may have less impact, which is the reason why both estimations of the increase of the skin depth agree. However, higher densities of FIB-cut trenches should result in this effect being more significant. As such, resistivity and ESR measurements may be affected differently by such damages, which can result in a discrepancy of both estimates. Our results are in agreement with our proposed scenario for the X/R development, stating that the impact of the surface on the ESR spectra can be largely suppressed by introducing FIB-cut trenches into the sample.

APPENDIX C: ANALYSIS OF THE SPIN-LATTICE RELAXATION

Due to our ESR being a continuous wave experiment, the estimation of the spin-lattice relaxation T_1 is an indirect measurement. We extract T_1 from the analysis of the ESR intensity I as a function of the microwave power P for fixed temperature T. We followed the steps as outlined in detail in [82], Chap. 13, Sec. C (p. 589). Assuming that the Bloch equations are valid and the broadening of the Gd^{3+} ESR line shape is homogeneous, T_1 can be expressed as

$$T_1 = \frac{\Delta H}{\gamma g}\,\frac{s^{-1} - 1}{H_1^2}, \tag{C1}$$

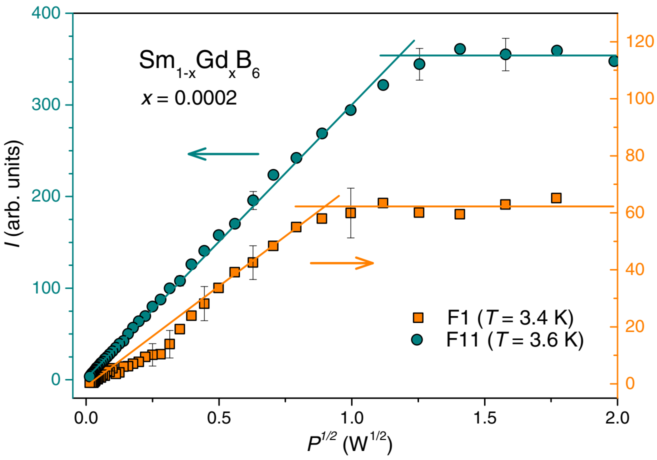

FIG. 7. ESR Intensity I as a function of the square root of the microwave power P for Sm$_{1-x}$Gd$_x$B$_6$ ($x = 0.0002$) F1 and F11. The solid lines are guides to the eye and indicate with their crossing points our estimation for the saturation power.

where γ is the gyromagnetic factor, g the ESR g-value, ΔH the ESR linewidth, and s the saturation term. The microwave magnetic field H_1 applied on the sample can be expressed as $H_1^2 = KP$, where K is a constant that depends on the microwave cavity and P is the microwave power (in W). Since K is always close to unity, a good approximation is to assume $K = 1$ Oe^2/W.

The saturation term s can be expressed as

$$s^{-3/2} = \left[\frac{\lim_{H_1\to 0}(I'/H_1)}{I'/H_1}\right] \propto \left[\frac{\lim_{H_1\to 0}(I'/\sqrt{P})}{I'/\sqrt{P}}\right], \qquad \text{(C2)}$$

where I' is the ESR intensity per microwave power P. One can see from Eq. (C2) that the saturation of the ESR spectrum can be obtained by analyzing the ESR intensity I as a function of H_1 or, more precisely, as a function of $\sqrt{P}$. Figure 7 shows the $\sqrt{P}$ dependence of I for F1 and F11. For our data, we assumed a saturation of the ESR spectrum as soon as the $\sqrt{P}$ dependence of I deviates from a straight line.

There are a few ways of extracting s and, therefore, obtaining T_1. The most common one is to analyze the saturation of the ESR spectrum, in which $s \to 2/3$. Assuming $s = 2/3$, Eq. (C1) can be rewritten as

$$T_1 = \frac{1.1371.10^{-7}\Delta H}{gP}. \qquad \text{(C3)}$$

Due to a few approximations, the extracted T_1 from our data will have significant error bars. Nevertheless, as shown in

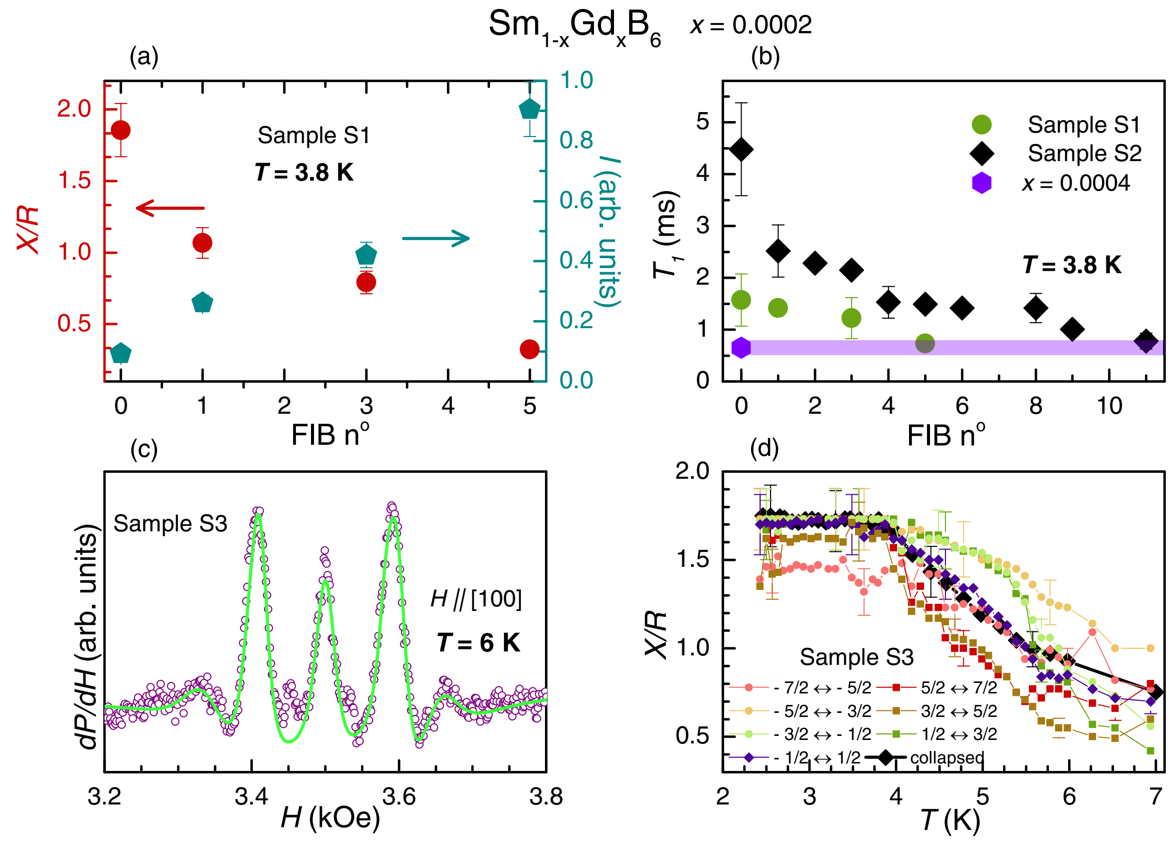

FIG. 8. (a) ESR Intensity I, X/R parameter and (b) T_1 as a function of the number of FIB-cut trenches at $T = 3.8$ K for sample S1. FIB number 0 denotes the sample without FIB-cut trenches. We also show T_1 for samples S2 and $x = 0.0004$ for a better comparison. (c) Gd^{3+} ESR spectrum at $T = 6$ K. The green solid line is a fitting as described in the main text. (d) X/R T dependence for H applied parallel to the [100] direction for sample S3. We also show the X/R T dependence for the Gd^{3+} collapsed spectrum. The solid lines in (d) are guides to the eye.

the main text, we can see a clear tendency of T_1 as a function of the number of FIB-cut trenches on the $x = 0.0002$ sample.

APPENDIX D: SAMPLE DEPENDENCE

To analyze the sample dependence, we also made FIB-cut trenches in sample S1. Figures 8(a) and 8(b) summarize the obtained results. As shown in Fig. 8(a), less FIB-cut trenches were necessary to recover a localized character of the Gd^{3+} ESR spectrum for sample S1 as compared to sample S2 (Fig. 4). The T_1 FIB-number dependence, which is shown in Fig. 8(b), shows the same qualitative behavior as sample S2.

For the samples without FIB-cut trenches, T_1 is smaller for sample S1 when compared with sample S2. Interestingly, this is also the case for the X/R parameter. Nonetheless, both samples show the same qualitative behavior: T_1 merges to the value seen for $x = 0.0004$, and the Gd^{3+} ESR localized-like character is recovered as a function of progressive FIB cutting.

One possible explanation for this sample dependence is the introduction of additional relaxation channels when a very small quantity of disorder is introduced into the system. Naturally, we should expect that samples with more disorder may not show the diffusive asymmetry of the Gd^{3+} ESR line shape, even with, nominally, the same Gd^{3+} content. T_1 appears to qualitatively capture such changes.

As a complement, we also investigated the T dependence of the diffusive asymmetry of the Gd^{3+} ESR spectra for applied magnetic field H parallel to the [100] direction. For this experiment, we used another sample out of the same batch, which we will call sample S3. Instead of just simulating the Gd^{3+} spectra, we fitted the seven lines, using Eq. (1), for extracting the general tendency of the X/R parameter. Due to the superposition of the different Gd^{3+} fine-structure resonances, a certain range of X/R is expected for a given temperature. However, one reliable aspect of this analysis is the general trend of the X/R parameter for each line, i.e., each line tends to have a localized-like character at higher temperatures.

Figure 8(c) shows the Gd^{3+} ESR spectrum at $T = 6$ K and Fig. 8(d) the obtained X/R for each line. As a matter of comparison, we also show the X/R T dependence for the Gd^{3+} ESR spectrum when the sample is turned by 30° away from the [001] towards the [110] direction (collapsed spectrum) in Fig. 8(d). Note that, similarly to the other samples, we again observe a X/R saturation at low temperatures.

[1] K. V. Klitzing, G. Dorda, and M. Pepper, New Method for High-Accuracy Determination of the Fine-Structure Constant Based on Quantized Hall Resistance, Phys. Rev. Lett. **45**, 494 (1980).

[2] M. Z. Hasan and C. L. Kane, *Colloquium:* Topological insulators, Rev. Mod. Phys. **82**, 3045 (2010).

[3] S. M. Young, S. Zaheer, J. C. Y. Teo, C. L. Kane, E. J. Mele, and A. M. Rappe, Dirac Semimetal in Three Dimensions, Phys. Rev. Lett. **108**, 140405 (2012).

[4] B. Yan and C. Felser, Topological materials: Weyl semimetals, Annu. Rev. Condens. Matter Phys. **8**, 337 (2017).

[5] K. Manna, Y. Sun, L. Muechler, J. Kübler, and C. Felser, Heusler, weyl and berry, Nat. Rev. Mater. **3**, 244 (2018).

[6] S.-Y. Xu, M. Neupane, C. Liu, D. Zhang, A. Richardella, L. A. Wray, N. Alidoust, M. Leandersson, T. Balasubramanian, J. Sánchez-Barriga *et al.*, Hedgehog spin texture and Berrys phase tuning in a magnetic topological insulator, Nat. Phys. **8**, 616 (2012).

[7] Z. Wang, A. Alexandradinata, R. J. Cava, and B. A. Bernevig, Hourglass fermions, Nature (London) **532**, 189 (2016).

[8] M. Dzero, K. Sun, V. Galitski, and P. Coleman, Topological Kondo Insulators, Phys. Rev. Lett. **104**, 106408 (2010).

[9] V. Alexandrov, M. Dzero, and P. Coleman, Cubic Topological Kondo Insulators, Phys. Rev. Lett. **111**, 226403 (2013).

[10] M. Dzero, J. Xia, V. Galitski, and P. Coleman, Topological Kondo insulators, Annu. Rev. Condens. Matter Phys. **7**, 249 (2016).

[11] C. Guo, F. Wu, Z. Wu, M. Smidman, C. Cao, A. Bostwick, C. Jozwiak, E. Rotenberg, Y. Liu, F. Steglich *et al.*, Evidence for Weyl fermions in a canonical heavy-fermion semimetal YbPtBi, Nat. Commun. **9**, 4622 (2018).

[12] S. Paschen and Q. Si, Quantum phases driven by strong correlations, Nat. Rev. Phys. **3**, 9 (2021).

[13] P. F. S. Rosa and Z. Fisk, in *Bulk and Surface Properties of SmB_6, in Rare-Earth Borides*, edited by D. S. Inosov (Jenny Stanford Publishing, Singapore, 2021).

[14] L. Li, K. Sun, C. Kurdak, and J. W. Allen, Emergent mystery in the kondo insulator samarium hexaboride, Nat. Rev. Phys. **2**, 463 (2020).

[15] D. J. Kim, J. Xia, and Z. Fisk, Topological surface state in the Kondo insulator samarium hexaboride, Nat. Mater. **13**, 466 (2014).

[16] D. J. Kim, S. Thomas, T. Grant, J. Botimer, Z. Fisk, and J. Xia, Surface Hall effect and nonlocal transport in SmB_6: Evidence for surface conduction, Sci. Rep. **3**, 3150 (2013).

[17] W. T. Fuhrman, J. Leiner, P. Nikolić, G. E. Granroth, M. B. Stone, M. D. Lumsden, L. DeBeer-Schmitt, P. A. Alekseev, J.-M. Mignot, S. M. Koohpayeh, P. Cottingham, W. A. Phelan, L. Schoop, T. M. McQueen, and C. L. Broholm, Interaction Driven Subgap Spin Exciton in the Kondo Insulator SmB_6, Phys. Rev. Lett. **114**, 036401 (2015).

[18] M. Neupane, N. Alidoust, S.-Y. Xu, T. Kondo, Y. Ishida, D. J. Kim, C. Liu, I. Belopolski, Y. J. Jo, T.-R. Chang, H.-T. Jeng, T. Durakiewicz, L. Balicas, H. Lin, A. Bansil, S. Shin, Z. Fisk, and M. Z. Hasan, Surface electronic structure of the topological Kondo-insulator candidate correlated electron system SmB_6, Nat. Commun. **4**, 2991 (2013).

[19] J. Jiang, S. Li, T. Zhang, Z. Sun, F. Chen, Z. R. Ye, M. Xu, Q. Q. Ge, S. Y. Tan, X. H. Niu, M. Xia, B. P. Xie, Y. F. Li, X. H. Chen, H. H. Wen, and D. L. Feng, Observation of possible topological in-gap surface states in the Kondo insulator SmB_6 by photoemission, Nat. Commun. **4**, 3010 (2013).

[20] S. Suga, K. Sakamoto, T. Okuda, K. Miyamoto, K. Kuroda, A. Sekiyama, J. Yamaguchi, H. Fujiwara, A. Irizawa, T. Ito, S. Kimura, T. Balashov, W. Wulfhekel, S. Yeo, F. Iga, and

S. Imada, Spin-polarized angle-resolved photoelectron spectroscopy of the so-predicted Kondo topological insulator SmB$_6$, J. Phys. Soc. Jpn. **83**, 014705 (2014).

[21] N. Xu, P. K. Biswas, J. H. Dil, R. S. Dhaka, G. Landolt, S. Muff, C. E. Matt, X. Shi, N. C. Plumb, M. Radović, E. Pomjakushina, K. Conder, A. Amato, S. V. Borisenko, R. Yu, H. M. Weng, Z. Fang, X. Dai, J. Mesot, H. Ding *et al.*, Direct observation of the spin texture in SmB$_6$ as evidence of the topological Kondo insulator, Nat. Commun. **5**, 4566 (2014).

[22] S. Wolgast, C. Kurdak, K. Sun, J. W. Allen, D.-J. Kim, and Z. Fisk, Low-temperature surface conduction in the Kondo insulator SmB$_6$, Phys. Rev. B **88**, 180405(R) (2013).

[23] M. Sundermann, H. Yavas, K. Chen, D. J. Kim, Z. Fisk, D. Kasinathan, M. W. Haverkort, P. Thalmeier, A. Severing, and L. H. Tjeng, 4f Crystal Field Ground State of the Strongly Correlated Topological Insulator SmB$_6$, Phys. Rev. Lett. **120**, 016402 (2018).

[24] Y. S. Eo, A. Rakoski, J. Lucien, D. Mihaliov, C. Kurdak, P. F. S. Rosa, and Z. Fisk, Transport gap in SmB$_6$ protected against disorder, Proc. Natl. Acad. Sci. USA **116**, 12638 (2019).

[25] Y. S. Eo, S. Wolgast, A. Rakoski, D. Mihaliov, B. Y. Kang, M. S. Song, B. K. Cho, M. C. Hatnean, G. Balakrishnan, Z. Fisk, S. R. Saha, X. Wang, J. Paglione, and C. Kurdak, Comprehensive surface magnetotransport study of SmB$_6$, Phys. Rev. B **101**, 155109 (2020).

[26] X. Zhang, N. P. Butch, P. Syers, S. Ziemak, R. L. Greene, and J. Paglione, Hybridization, Inter-Ion Correlation, and Surface States in the Kondo Insulator SmB$_6$, Phys. Rev. X **3**, 011011 (2013).

[27] P. Syers, D. Kim, M. S. Fuhrer, and J. Paglione, Tuning Bulk and Surface Conduction in the Proposed Topological Kondo Insulato SmB$_6$, Phys. Rev. Lett. **114**, 096601 (2015).

[28] S. Lee, X. Zhang, Y. Liang, S. W. Fackler, J. Yong, X. Wang, J. Paglione, R. L. Greene, and I. Takeuchi, Observation of the Superconducting Proximity Effect in the Surface State of SmB$_6$ Thin Films, Phys. Rev. X **6**, 031031 (2016).

[29] L. Jiao, S. Rößler, D. J. Kim, L. H. Tjeng, Z. Fisk, F. Steglich, and S. Wirth, Additional energy scale in SmB$_6$ at low temperature, Nat. Commun. **7**, 13762 (2016).

[30] L. Jiao, S. Rößler, D. Kasinathan, P. F. S. Rosa, C. Guo, H. Yuan, C.-X. Liu, Z. Fisk, F. Steglich, and S. Wirth, Magnetic and defect probes of the SmB$_6$ surface state, Sci. Adv. **4**, eaau4886 (2018).

[31] H. Pirie, Y. Liu, A. Soumyanarayanan, P. Chen, Y. He, M. M. Yee, P. F. S. Rosa, J. D. Thompson, D.-J. Kim, Z. Fisk, X. Wang, J. Paglione, D. K. Morr, M. H. Hamidian, and J. E. Hoffman, Imaging emergent heavy Dirac fermions of a topological kondo insulator, Nat. Phys. **16**, 52 (2020).

[32] C. E. Matt, H. Pirie, A. Soumyanarayanan, Y. He, M. M. Yee, P. Chen, Y. Liu, D. T. Larson, W. S. Paz, J. J. Palacios, M. H. Hamidian, and J. E. Hoffman, Consistency between ARPES and STM measurements on SmB$_6$, Phys. Rev. B **101**, 085142 (2020).

[33] P. Hlawenka, K. Siemensmeyer, E. Weschke, A. Varykhalov, J. Sánchez-Barriga, N. Y. Shitsevalova, A. V. Dukhnenko, V. B. Filipov, S. Gabáni, K. Flachbart, O. Rader, and E. D. L. Rienks, Samarium hexaboride is a trivial surface conductor, Nat. Commun. **9**, 517 (2018).

[34] H. Herrmann, P. Hlawenka, K. Siemensmeyer, E. Weschke, J. Sánchez-Barriga, A. Varykhalov, N. Y. Shitsevalova, A. V. Dukhnenko, V. B. Filipov, S. Gabáni, K. Flachbart, O. Rader, M. Sterrer, and E. D. L. Rienks, Contrast reversal in scanning tunneling microscopy and its implications for the topological classification of SmB$_6$, Adv. Mater. **32**, 1906725 (2020).

[35] M. E. Valentine, S. Koohpayeh, W. A. Phelan, T. M. McQueen, P. F. S. Rosa, Z. Fisk, and N. Drichko, Breakdown of the kondo insulating state in SmB$_6$ by introducing Sm vacancies, Phys. Rev. B **94**, 075102 (2016).

[36] M. E. Valentine, S. Koohpayeh, W. A. Phelan, T. M. McQueen, P. F. S. Rosa, Z. Fisk, and N. Drichko, An effect of sm vacancies on the hybridization gap in topological kondo insulator candidate SmB$_6$, Physica B **536**, 60 (2018).

[37] S. Sen, N. S. Vidhyadhiraja, E. Miranda, V. Dobrosavljević, and W. Ku, Fragility of the Kondo insulating gap against disorder: Relevance to recent puzzles in topological Kondo insulators, Phys. Rev. Research **2**, 033370 (2020).

[38] M. Abele, X. Yuan, and P. S. Riseborough, Topological nonmagnetic impurity states in topological Kondo insulators, Phys. Rev. B **101**, 094101 (2020).

[39] J. C. Souza, P. F. S. Rosa, J. Sichelschmidt, M. Carlone, P. A. Venegas, M. O. Malcolms, P. M. Menegasso, R. R. Urbano, Z. Fisk, and P. G. Pagliuso, Metallic islands in the Kondo insulator SmB$_6$, Phys. Rev. Research **2**, 043181 (2020).

[40] M. C. Hatnean, M. R. Lees, D. M. Paul, and G. Balakrishnan, Large, high quality single-crystals of the new topological Kondo insulator, SmB$_6$, Sci. Rep. **3**, 3071 (2013).

[41] G. Li, Z. Xiang, F. Yu, T. Asaba, B. Lawson, P. Cai, C. Tinsman, A. Berkley, S. Wolgast, Y. S. Eo *et al.*, Two-dimensional Fermi surfaces in Kondo insulator SmB$_6$, Science **346**, 1208 (2014).

[42] B. Tan, Y.-T. Hsu, B. Zeng, M. C. Hatnean, N. Harrison, Z. Zhu, M. Hartstein, M. Kiourlappou, A. Srivastava, M. Johannes *et al.*, Unconventional Fermi surface in an insulating state, Science **349**, 287 (2015).

[43] W. A. Phelan, S. M. Koohpayeh, P. Cottingham, J. A. Tutmaher, J. C. Leiner, M. D. Lumsden, C. M. Lavelle, X. P. Wang, C. Hoffmann, M. A. Siegler, N. Haldolaarachchige, D. P. Young, and T. M. McQueen, On the chemistry and physical properties of flux and floating zone grown SmB$_6$ single crystals, Sci. Rep. **6**, 20860 (2016).

[44] S. M. Thomas, X. Ding, F. Ronning, V. Zapf, J. D. Thompson, Z. Fisk, J. Xia, and P. F. S. Rosa, Quantum Oscillations in Flux-Grown SmB$_6$ with Embedded Aluminum, Phys. Rev. Lett. **122**, 166401 (2019).

[45] S. Gheidi, K. Akintola, K. S. Akella, A. M. Côté, S. R. Dunsiger, C. Broholm, W. T. Fuhrman, S. R. Saha, J. Paglione, and J. E. Sonier, Intrinsic Low-Temperature Magnetism in SmB$_6$, Phys. Rev. Lett. **123**, 197203 (2019).

[46] W. T. Fuhrman, J. R. Chamorro, P. Alekseev, J.-M. Mignot, T. Keller, J. A. Rodriguez-Rivera, Y. Qiu, P. Nikolić, T. M. McQueen, and C. L. Broholm, Screened moments and extrinsic in-gap states in samarium hexaboride, Nat. Commun. **9**, 1539 (2018).

[47] M. V. Crivillero, M. König, J. C. Souza, P. G. Pagliuso, J. Sichelschmidt, P. F. S. Rosa, Z. Fisk, and S. Wirth, Systematic manipulation of the surface conductivity of SmB$_6$, Phys. Rev. Research **3**, 023162 (2021).

[48] G. Feher and A. Kip, Electron spin resonance absorption in metals. I. Experimental, Phys. Rev. **98**, 337 (1955).

[49] G. Lesseux, T. Garitezi, P. Rosa, C. Jesus, S. Oseroff, J. Sarrao, Z. Fisk, R. Urbano, P. Pagliuso, and C. Rettori, Unusual diffusive effects on the ESR of Nd^{3+} ions in the tunable topologically nontrivial semimetal YBiPt, J. Phys.: Condens. Matter **28**, 125601 (2016).

[50] S. Demishev, M. Gilmanov, A. Samarin, A. Semeno, N. Sluchanko, N. Samarin, A. Bogach, N. Y. Shitsevalova, V. Filipov, M. Karasev *et al.*, Magnetic resonance probing of ground state in the mixed valence correlated topological insulator SmB_6, Sci. Rep. **8**, 7125 (2018).

[51] M. Hemmida, H.-A. Krug von Nidda, B. Miksch, L. L. Samoilenko, A. Pustogow, S. Widmann, A. Henderson, T. Siegrist, J. A. Schlueter, A. Loidl, and M. Dressel, Weak ferromagnetism and glassy state in κ-(BEDT- TTF)$_2$ Hg (SCN)$_2$ Br, Phys. Rev. B **98**, 241202(R) (2018).

[52] P. G. Pagliuso, C. Rettori, J. L. Sarrao, A. Cornelius, M. F. Hundley, Z. Fisk, and S. B. Oseroff, Electron spin resonance of Gd^{3+} and Nd^{3+} in $LuInA_4$ (A= Cu, Ni), Phys. Rev. B **60**, 13515 (1999).

[53] L. Walmsley, S. Rolla, and C. Rettori, Spin resonance lineshape and c-axis resistivity in $SbCl_5$-GICs, Synth. Met. **23**, 305 (1988).

[54] S. Barnes, Theory of electron spin resonance of magnetic ions in metals, Adv. Phys. **30**, 801 (1981).

[55] F. J. Dyson, Electron spin resonance absorption in metals. II. Theory of electron diffusion and the skin effect, Phys. Rev. **98**, 349 (1955).

[56] C. P. Poole and H. A. Farach, *Relaxation in Magnetic Resonance*, Vol. 19 (Elsevier, Amsterdam, 1971).

[57] A. Abragam and B. Bleaney, *Electron Paramagnetic Resonance of Transition Ions* (Oxford University Press, Oxford, 2012).

[58] R. Orbach, On the theory of spin-lattice relaxation in paramagnetic salts, Proc. Phys. Soc. **77**, 821 (1961).

[59] D. A. Garanin and E. M. Chudnovsky, Angular momentum in spin-phonon processes, Phys. Rev. B **92**, 024421 (2015).

[60] J. J. Nakane and H. Kohno, Angular momentum of phonons and its application to single-spin relaxation, Phys. Rev. B **97**, 174403 (2018).

[61] J. H. Pifer and R. Magno, Conduction-electron spin resonance in a lithium film, Phys. Rev. B **3**, 663 (1971).

[62] J. Souza, G. Lesseux, R. Urbano, C. Rettori, and P. Pagliuso, Diffusive-like effects and possible non trivial local topology on the half-Heusler YPdBi compound, AIP Adv. **8**, 055713 (2018).

[63] D. A. Garanin, Towards a microscopic understanding of the phonon bottleneck, Phys. Rev. B **75**, 094409 (2007).

[64] P. F. S. Rosa and Z. Fisk, Flux methods for growth of intermetallic single crystals, in *Crystal Growth of Intermetallics*, edited by P. Gille and Y. Grin (De Gruyter, Berlin, 2018), pp. 49–60.

[65] A. Amon, I. Zelenina, P. Simon, M. Bobnar, M. Naumann, E. Svanidze, F. Arnold, H. Borrmann, U. Burkhardt, W. Schnelle *et al.*, Tracking aluminium impurities in single crystals of the heavy-fermion superconductor UBe_{13}, Sci. Rep. **8**, 10654 (2018).

[66] G. Reuter and E. Sondheimer, The theory of the anomalous skin effect in metals, Proc. R. Soc. London A **195**, 336 (1948).

[67] Z. Liu, L. Yang, S.-C. Wu, C. Shekhar, J. Jiang, H. Yang, Y. Zhang, S.-K. Mo, Z. Hussain, B. Yan *et al.*, Observation of unusual topological surface states in half-Heusler compounds LnPtBi (Ln= Lu, Y), Nat. Commun. **7**, 12924 (2016).

[68] C. Rettori, D. Davidov, P. Chaikin, and R. Orbach, Magnetic Resonance of a Localized Magnetic Moment in the Superconducting State: $LaRu_2$:Gd, Phys. Rev. Lett. **30**, 437 (1973).

[69] U. Engel, K. Baberschke, G. Koopmann, S. Hüfner, and M. Wilhelm, Local moment spin resonance in a superconductor, Solid State Commun. **12**, 977 (1973).

[70] N. Alekseevskii, I. Garufullin, B. Kochelaev, and E. Kharakhash'Yan, Electron resonance with localized magnetic moments of Er in superconducting La, J. Exp. Theor. Phys. **18**, 323 (1973).

[71] D. Davidov, C. Rettori, and H. Kim, Electron-spin resonance of a localized moment in the superconducting state: BRu_2: Gd (B= La, Ce, Th), Phys. Rev. B **9**, 147 (1974).

[72] R. Orbach, Electron spin resonance in superconductors, Phys. Lett. A **47**, 281 (1974).

[73] V. Sacksteder, T. Ohtsuki, and K. Kobayashi, Modification and Control of Topological Insulator Surface States Using Surface Disorder, Phys. Rev. Applied **3**, 064006 (2015).

[74] V. B. Zabolotnyy, K. Fürsich, R. J. Green, P. Lutz, K. Treiber, C.-H. Min, A. V. Dukhnenko, N. Y. Shitsevalova, V. B. Filipov, B. Y. Kang, B. K. Cho, R. Sutarto, F. He, F. Reinert, D. S. Inosov, and V. Hinkov, Chemical and valence reconstruction at the surface of SmB_6 revealed by means of resonant soft x-ray reflectometry, Phys. Rev. B **97**, 205416 (2018).

[75] W. T. Fuhrman, J. C. Leiner, J. W. Freeland, M. van Veenendaal, S. M. Koohpayeh, W. A. Phelan, T. M. McQueen, and C. Broholm, Magnetic dichroism in the Kondo insulator SmB_6, Phys. Rev. B **99**, 020401(R) (2019).

[76] Y. S. Eo, A. Rakoski, S. Sinha, D. Mihaliov, W. T. Fuhrman, S. R. Saha, P. F. S. Rosa, Z. Fisk, M. C. Hatnean, G. Balakrishnan, J. R. Chamorro, W. A. Phelan, S. M. Koohpayeh, T. M. McQueen, B. Kang, M.-S. Song, B. Cho, M. S. Fuhrer, J. Paglione, and Ç. Kurdak, Bulk transport paths through defects in floating zone and Al flux grown SmB_6, Phys. Rev. Materials **5**, 055001 (2021).

[77] M. V. Crivillero, S. Rößler, H. Borrmann, H. Dawczak-Debicki, P. F. S. Rosa, Z. Fisk, and S. Wirth, Phase stability of SmB_6, Phys. Rev. Materials **5**, 044204 (2021).

[78] J. Lawrence, T. Graf, M. Hundley, D. Mandrus, J. Thompson, A. Lacerda, M. Torikachvili, J. Sarrao, and Z. Fisk, Kondo hole behavior in $Ce_{0.97}$ $La_{0.03}$ Pd_3, Phys. Rev. B **53**, 12559 (1996).

[79] J. Holanda, D. Maior, A. Azevedo, and S. Rezende, Detecting the phonon spin in magnon–phonon conversion experiments, Nat. Phys. **14**, 500 (2018).

[80] F. Grusdt, N. Y. Yao, D. Abanin, M. Fleischhauer, and E. Demler, Interferometric measurements of many-body topological invariants using mobile impurities, Nat. Commun. **7**, 11994 (2016).

[81] P. J. Moll, Focused ion beam microstructuring of quantum matter, Annu. Rev. Condens. Matter Phys. **9**, 147 (2018).

[82] C. P. Poole, *Electron Spin Resonance: A Comprehensive Treatise on Experimental Techniques* (Courier, North Chelmsford, MA, 1996).